Review article

Novel spintronic effects in two-dimensional van der Waals heterostructures

Check for updates

Zhiyuan Zhao[1], Yijie Lin[1] & Ahmet Avsar[1,2,3] ✉

Precise engineering of spin interfaces is essential for the development of spintronic devices. Two-dimensional vdW heterostructures enable atomically sharp interfaces that facilitate exploration of fundamental spin phenomena. Moreover, the discovery of two-dimensional magnetic materials has accelerated the field, leading to novel devices and spin effects. This review highlights recent advancements in vdW interfacial spin physics, innovative device structures, and emerging moiré-induced topological effects, with implications for future spintronic applications.

The advancement of contemporary electronics has heavily relied on complementary metal-oxide-semiconductor (CMOS) technology. This foundational technology is integral to the manufacture of nearly all integrated circuits found in devices like computers and mobile phones. Despite significant improvements in CMOS integrated circuits over the past fifty years, issues related to scaling, such as high standby power dissipation, have emerged as the technology approaches its theoretical limits. To keep pace with rapid innovation—demanding enhanced data storage and processing capabilities for applications like blockchain-based cryptocurrencies and autonomous vehicles—new types of electronic devices must be developed. These next-generation devices will need to employ unconventional state variables, materials, and architectures. One promising direction for the post-CMOS era involves utilizing electron spin for data processing and storage[1–3]. However, developing these devices involves overcoming challenges related to materials and interfaces[4].

A major breakthrough in materials science was the discovery of the ambipolar electric field effect in graphene (Gr), which spurred intensive research into atomically thin materials[5]. The significance of two-dimensional (2D) materials expanded with the identification of materials beyond graphene[6–8], the development of heterostructures composed of these materials, and the creation of twisted artificial structures[9]. Many of these 2D materials show great promise for spintronics, particularly when incorporated into designable van der Waals (vdW) heterostructures[4,10–16]. These vdW heterostructures allow for versatile artificial constructs with nearly arbitrary modulation of chemical compositions and electronic structures, without the strict lattice-matching requirements typical of conventional heterostructures. Unlike conventional heterostructures, which often suffer from issues such as crystal defects, local strains, and interface dipoles, vdW heterostructures enable the creation of clean, atomically sharp interfaces[17].

These well-defined interfaces in vdW heterostructures are especially crucial for spintronics, as they facilitate proximity studies and mitigate spin dephasing effects commonly encountered in conventional heterostructures. For instance, the precise modulation of interfaces in vdW materials significantly impacts various spin-orbit effects, including ferromagnetism[18], interlayer coupling[19,20], and spin-orbit coupling (SOC)[10,15]. As summarised in Fig. 1, recent developments have optimized interfaces and proximity effects to induce key parameters such as the Curie temperature (T_c)[21], exchange bias[20], spin-lifetime anisotropy[22], and spin-orbit torques (SOTs)[23,24] in vdW heterostructures. Additionally, novel spin-dependent phenomena such as ferromagnetism[25], SOC[26], superconductivity[27,28], and nano-ampere level current-driven magnetic switching[29,30] have been induced through twist engineering in various Moiré systems. These advancements highlight the potential of interface engineering in vdW heterostructures for achieving energy-efficient spin manipulation.

In this review, we explore the latest developments in vdW interfacial physics, focusing on how spin transport and spin-orbit effects are modulated through vdW interface engineering. We examine how these advanced heterostructures are integrated into traditional magnetic random-access memory (MRAM) architectures, including vertical magnetic tunnel junctions (MTJs), lateral spin valves, and SOTs. Additionally, we discuss unconventional quantum effects that emerge in vdW materials and device architectures, which are not observable in conventional materials and are often overlooked in earlier spintronics reviews. This review aims to provide a comprehensive overview of these recent advancements and their implications for optimizing spin-orbit effects and achieving energy-efficient spin transport.

Interface engineering of interlayer coupling in vdW heterostructures

Unlike traditional bulk materials, where the characteristic lengths of proximity effects are typically much smaller than the sample size and thus often disregarded, atomically thin vdW heterostructures offer unique

[1]Department of Materials Science and Engineering, National University of Singapore, Singapore, Singapore. [2]Centre for Advanced 2D Materials, National University of Singapore, Singapore, Singapore. [3]Department of Physics, National University of Singapore, Singapore, Singapore. ✉e-mail: aavsar@nus.edu.sg
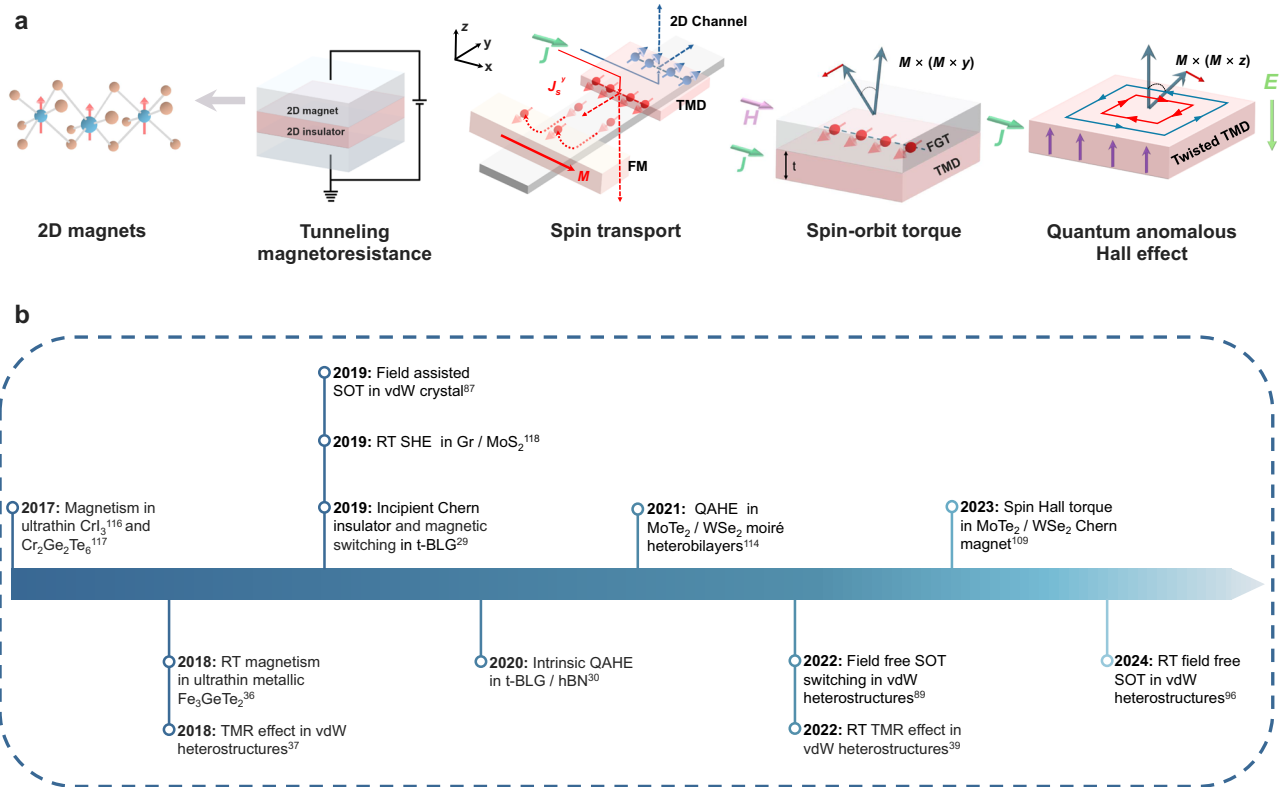
Fig. 1 | Interface engineering in van der Waals spintronic applications.
a Application of van der Waals materials in spintronics devices with different device architectures. The coordinate axes are shown in (**a**). In the schematic diagrams of the spin-orbit torque and quantum anomalous Hall effect in (**a**), the blue arrows represent magnetic moments, the red arrows indicate the spin torque generated by the interaction between the magnetic moments and the spin-polarized current, and the black dashed circles indicate the deflection of the magnetic moment under the influence of the spin torques. **b** The recent milestones of spintronics in van der Waals materials and heterostructures. The timeline shows the development of interface-dependent spin-orbit effects in vdW material systems within different types of MRAM architectures.
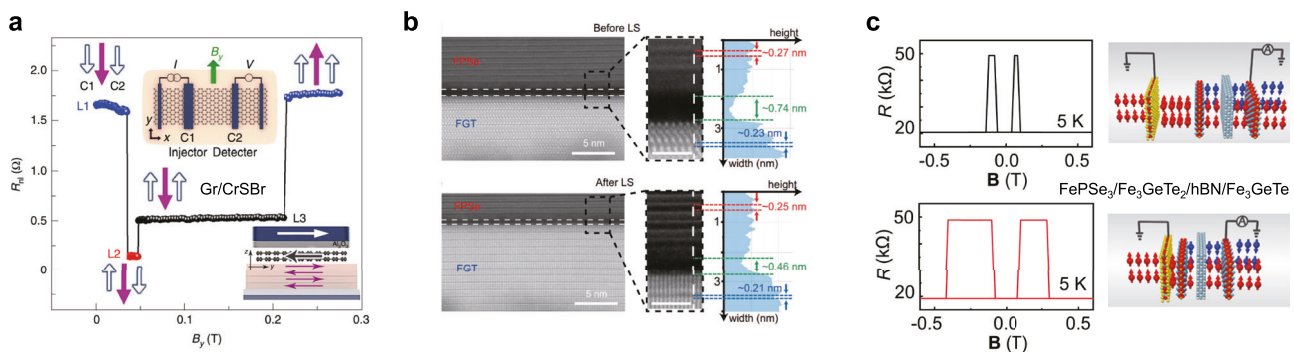

Fig. 2 | Interface engineering of interlayer coupling in vdW heterostructures.
a Non-local spin valve measurement in BLG/CrSBr heterostructure. Device structure and magnetization switching configuration are shown in the inset figure.
b STEM cross-sectional image (left) and intensity distribution along the white dashed line (right). The top images depict the vdW interface before the application of high-pressure laser shock, while the bottom image illustrates the vdW interface after the application of high-pressure laser shock, demonstrating a decreased interface spacing. **c** Tunneling resistance of the FePSe$_3$/Fe$_3$GeTe$_2$/hBN/Fe$_3$GeTe$_2$ MTJ before (upper) and after (bottom) applying a high-pressure laser shock, with magnetic field B applied parallel to the Fe$_3$GeTe$_2$ c-axis. **a** Reprinted with permission from ref. 18. Copyright 2021 Springer Nature. **b**, **c** Reprinted with permission from ref. 20. Copyright 2023 Springer Nature.

advantages for studying these effects[16]. In these ultrathin materials, proximity effects become significant relative to their thickness, making them highly promising for spintronic applications. The quality of interfaces and the precise control of interlayer distances are critical factors influencing these proximity effects. Ghiasi et al. demonstrated that placing bilayer graphene (BLG) on magnetic CrSBr introduces ferromagnetism into the otherwise non-magnetic BLG[18], as shown in Fig. 2a. A non-local spin valve based on the BLG/CrSBr heterostructure exhibits an additional resistance level due to the proximity effect of CrSBr, alongside the two non-local

resistance levels associated with the parallel and antiparallel magnetization alignment of the injector and detector cobalt electrodes. Similarly, proximity-induced magnetism has been reported in graphene due to Cr$_2$Ge$_2$Te$_6$, where the ferromagnetic exchange interaction significantly modifies spin transport and precession, leading to an anisotropic spin texture[31]. This underscores the importance of clean and well-defined interfaces in enabling spin–charge coupling and proximity magnetism. Moreover, the role of interlayer distance in proximity interactions is illustrated by the work of Huang et al.[20]. By applying high-pressure laser shocks
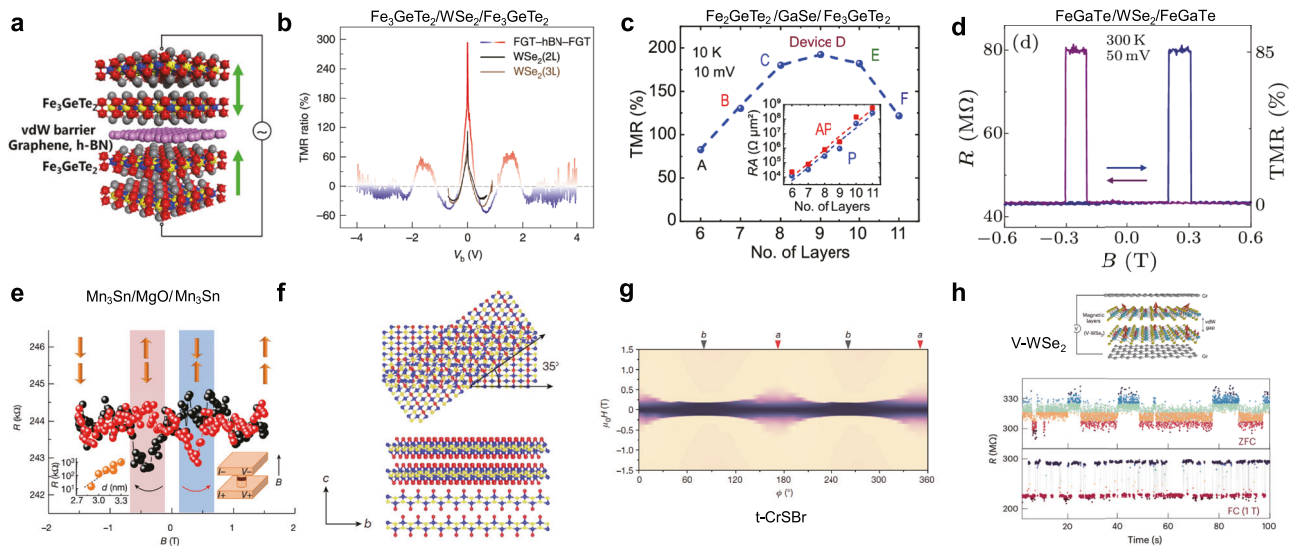
Fig. 3 | Tunneling magnetoresistance in van der Waals MTJs. a Schematic illustration of all van der Waals MTJ. **b** The back-gate voltage dependence of TMR ratio in Fe_3GeTe_2/hBN/Fe_3GeTe_2 and Fe_3GeTe_2/WSe_2/Fe_3GeTe_2. **c** TMR ratio of Fe_3GeTe_2/GaSe/Fe_3GeTe_2 MTJ plotted with the number of GaSe layers at 10 K with a bias voltage of 10 mV. **d** Room-temperature resistance (R) and TMR plotted as a function of magnetic field (B) of FeGaTe/WSe_2/FeGaTe MTJ at a constant bias voltage 50 mV. **e** The change of tunneling resistance of Mn_3Sn/MgO/Mn_3Sn MTJ with respect to magnetic field. **f** Schematic of twisted CrSBr bilayers. Top view and side view are shown in the top and bottom panels respectively. b and c crystal axes are denoted. The blue, yellow and red balls correspond to Cr, S and Br, respectively[48]. **g** Magnetic field orientation dependence of the tunnelling current in the a–b plane at 2 K, with a constant DC bias of 10 mV applied. The angles corresponding to the crystal axes are indicated by inverted triangles[48]. **h** The top panel illustrates the schematics of the device, comprising graphene-encapsulated, vanadium-doped WSe_2. The bottom panel depicts the time evolution of resistance change at 2 K and - 0.9 V. **a** Reprinted with permission from ref. 37. Copyright 2018 American Chemical Society. **b** Reprinted with permission from ref. 38. Copyright 2022 Springer Nature. **c** Reprinted with permission from ref. 39. Copyright 2023 Springer Nature. **d**, Reprinted with permission from ref. 43. Copyright 2022 Chinese Physical Society and IOP Publishing Ltd. **e** Reprinted with permission from ref. 44. Copyright 2023 Springer Nature. **f, g**, Reprinted with permission from ref. 48. Copyright 2024 Springer Nature. **h** Reprinted with permission from ref. 52. Copyright 2023 Springer Nature.

within the picosecond range, they were able to tune the vdW spacing in the $FePSe_3$/Fe_3GeTe_2 heterostructure as shown in Fig. 2b, enhancing the interlayer coupling and significantly increasing the exchange bias field from 29.2mT to 111.2mT[20]. Additionally, a high-quality MTJ device based on $FePSe_3$/Fe_3GeTe_2/hBN/Fe_3GeTe_2 displayed a 154% enhancement in the tunnelling magnetoresistance (TMR) ratio after pressure engineering as shown in Fig. 2c. These findings highlight how manipulating interlayer distance and interface quality can optimize proximity interactions and enhance device performance. The recent advancements in heterostructure fabrication techniques have enabled the achievement of ultra-clean interfaces[32,33]. Understanding the significance of clean interfaces and controlled interlayer distances is crucial for advancing the study and application of proximity effects in vdW heterostructures, which will be further explored in this review.

Tunneling magnetoresistance

The spin valve effect, characterized by the dependence of junction resistance on the orientation of the macroscopic magnetization of the ferromagnetic (FM) electrodes, has been a central focus of spintronics research due to its potential applications in many spintronic devices[34]. This effect can be realized in both vertical and lateral magnetic junctions. The TMR effect, which relies on spin-dependent tunnelling between ferromagnets in a vertical MTJ architecture, has been extensively studied and is used in solid-state devices, with the CoFeB/MgO structure being the main TMR configuration[12,35]. As the size of MTJs continues to scale down to increase device density, the essential annealing process (~ 400 °C) during device fabrication increases the likelihood of atomic mixing between different layers, increasing the risk of tunnel barrier failure, especially when the roughness of the layers is comparable to their thickness. The discovery of metallic vdW magnets[36] and high-quality layered tunnel barriers[37–39] presents all-vdW magnetic heterostructures as a promising platform for further enhancing MTJ functionalities. These atomically thin materials offer significant advantages, such

as minimizing defects related to dangling bonds, interface states, and interfacial alloy formation, and improving device morphology. As the 2D tunnel barrier thickness and lateral dimensions decrease, their atomic thinness, inertness, pinhole-free nature, and flexibility do not degrade compared to conventional TMR structures, making 2D-based vdW TMR devices highly promising for enhanced performance and reliability in scaled-down applications[12].

Van der Waals interfaces in MTJ architectures enable novel tunneling mechanisms and magnetoresistive effects, leading to unexpected device functionalities beyond those of traditional ferromagnetic MTJs. The first all vdW MTJ was realized in Fe_3GeTe_2/hBN/Fe_3GeTe_2 (Fig. 3a), achieving a maximum TMR ratio of 160% below an operating temperature of 180 K[37]. In all-vdW Fe_3GeTe_2/hBN/Fe_3GeTe_2 and Fe_3GeTe_2/WSe_2/Fe_3GeTe_2 MTJs, TMR values up to 300% with polarity inversion were achieved by manipulating the carrier spin polarization through applied voltage[38], as shown in Fig. 3b. Note that this spin polarization reversal is attributed to contributions from high-energy localized spin states in Fe_3GeTe_2 under bias voltage, which cannot be achieved under the same bias conditions in traditional MTJs[40–42]. TMR devices have used hBN[38], WSe_2[38], or GaSe[39] (Fig. 3c) as tunnel barriers in different studies, and all showed that the thickness of the non-magnetic barrier directly affects the achieved TMR values and their sign. The first room-temperature (RT) TMR was achieved by optimizing the selection of vdW ferromagnetic layers. For instance, fabricating FeGaTe/WSe_2/FeGaTe MTJs using FeGaTe, which has a Curie temperature of 380 K, resulted in a TMR ratio of up to 85% at RT[43], as shown in Fig. 3d. Another exciting advancement is the TMR effect observed using non-collinear antiferromagnetic (AFM) materials. Recently, RT-TMR signals were observed in Mn_3Sn/MgO/Mn_3Sn[44] and Mn_3Pt/MgO/Mn_3Pt[45] MTJs based on AFM films, as shown in Fig. 3e. Theoretical calculations indicate that the TMR effect in Mn_3Sn/MgO/Mn_3Sn is primarily introduced by the spin subbands and spin polarization associated with Mn_3Sn magnetic octupoles[44]. With an electric field perpendicular to the multilayer, electron redistribution

near the Fermi surface is expected, and the spin polarization of these electrons depends on the orientation of the magnetic octupole. The careful selection of vdW collinear AFMs could enhance the observed low TMR efficiencies, making it more suitable for applications.

The magnetic vdW material CrSBr exhibits layer-dependent magnetic order and anisotropic spin interactions along its crystallographic axes, making it a promising platform for spintronic research[46]. Its unique combination of magnetic anisotropy, thickness-dependent ordering, and twist engineering enables novel spintronic functionalities. For instance, twisting two CrSBr monolayers by 90° introduces multi-step magnetic switching with hysteresis, where the non-collinear spin texture can be precisely controlled by the magnitude and direction of an applied magnetic field[47]. Twist engineering has also led to breakthroughs in TMR devices. Y. Chen et al. demonstrated that twisting two bilayers of the 2D antiferromagnet CrSBr results in an over 700% nonvolatile TMR ratio at zero field, with the entire twisted stack serving as the tunnel barrier, as shown in Fig. 3f. When an external magnetic field is applied along the easy (or hard) magnetization axis of one flake, its magnetization becomes pinned, making it more difficult (or easier) to switch the magnetization of the other flake. This results in a twist-angle-dependent TMR ratio, as illustrated in Fig. 3g[48]. Beyond CrSBr, twist engineering has also been explored in CrI_3. In bilayer CrI_3 with a small twist angle, the coexistence of ferromagnetic and antiferromagnetic ground states has been observed, demonstrating the potential for creating complex magnetic configurations in twisted bilayer 2D magnets[49].

Lastly, due to their non-volatile storage capabilities and the ability to integrate storage with computation, TMR devices have recently garnered interest in emerging neural network computing[50]. Beyond the widely explored approach of embedding memory in processors, the probabilistic bits, which can be realized through various resistance fluctuation mechanisms—including magnetic fluctuations in unstable magnets—enable efficient logical computation with a reduced number of bits[51]. Recently, electrically tunable magnetic fluctuations have been observed in graphene/vanadium—doped WSe_2/graphene MTJs, where the vanadium-doped WSe_2 serves as the FM layer, exhibiting random telegraph noise and tunable magnetic fluctuations under applied voltage[52], as shown in Fig. 3h. Beyond V-doped WSe_2, the extensive library of TMDC materials is anticipated to offer a broader selection for use in neural network computing architectures.

Spin transport

Similar to vertical TMR devices, lateral spin valve devices are also frequently studied for extracting the spin transport properties of non-magnetic materials[10]. Among the various lateral device geometries, the non-local spin valve (NLSV) stands out as particularly significant as it can eliminate the spurious signals that could mimic the spin signal. An NLSV consists of a spin injector, transport channel, spin detector, and two reference electrodes, enabling the electrical injection, transport, manipulation, and detection of pure spin current within the channel, as illustrated in the inset of Fig. 4a. One of the main goals in this field is to achieve large non-local spin signals and long spin relaxation lengths (λ_s) at RT, which are required to realize compact spin circuits[53]. Among all materials, 2D graphene stands out for its exceptionally long-distance spin communication at RT[54], attributed to its weak SOC, which facilitates spin current propagation in complex circuit architectures[55]. For instance, D. Khokhriakov et al. demonstrated a spin logic circuit using graphene channels and a 3-fan input to achieve multi-state output spin signals and various spin logic operations[56]. However, the experimentally observed λ_s values in graphene remain considerably shorter than the theoretically predicted values. Pioneering work by M. Drogeler et al. indicates that factors such as the quality of the graphene/FM injector interface and fabrication residues may limit the attainment of these theoretical expectations[57].

Recent advancements in vdW ferromagnets have paved the way for the developing of entirely vdW materials-based spin valve devices. In these devices, vdW ferromagnets are integrated onto graphene channels using a dry-transfer method, effectively avoiding the introduction of magnetic
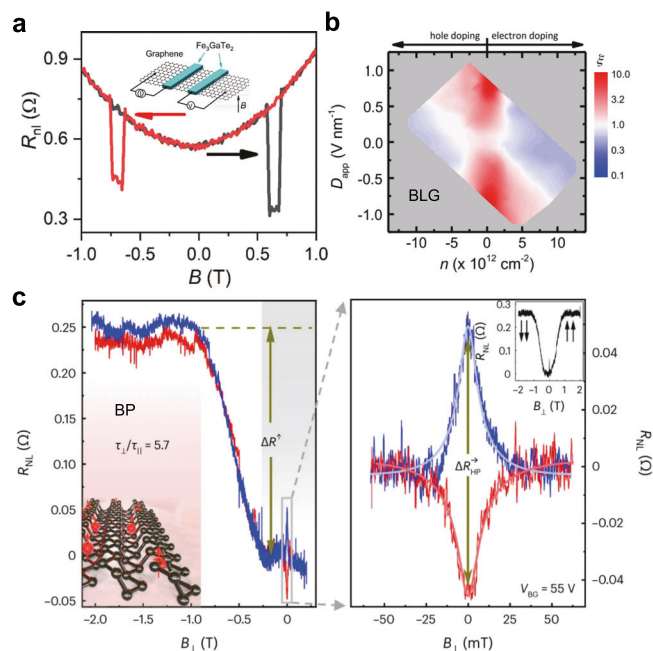
Fig. 4 | Spin transport behavior in van der Waals non-local spin valves. a Non-local spin valve signal as a function of perpendicular magnetic field in all-vdW Fe_3GaTe_2/graphene NLSV devices at 100 K. **b** Electric field and carrier density dependence of spin lifetime anisotropy in bilayer graphene. **c** Non-local spin valve signal plotted with perpendicular magnetic field in BP. The right panel is the magnified image of spin precession at magnetic field below 0.25 T. **a** Reprinted with permission from ref. 59. Copyright 2023 American Chemical Society. **b** Reprinted with permission from ref. 69. Copyright 2018 American Physical Society. **c** Reprinted with permission from ref. 71. Copyright 2024 Springer Nature.

impurities[58]. The atomically smooth interface between the vdW ferromagnetic electrodes and graphene helps to minimize spin-dependent scattering at the interface. The first RT all-vdW NLSV devices were realized using a Fe_3GaTe_2/graphene architecture[59]. Figure 4a illustrates the measured non-local resistance (R_{nl}) curve, where the magnetic field is applied perpendicular to the Fe_3GaTe_2 layer. Notably, the non-local spin valve signal is observable even at 320 K and remains robust at a low bias current of 1 μA. Additionally, varying the angle of the applied magnetic field during non-local measurements reveals that R_{nl} is linked to the significant perpendicular magnetic anisotropy of Fe_3GaTe_2. The NLSV signal is markedly enhanced when the magnetic field is aligned close to the perpendicular direction, indicating that the adjacent Fe_3GaTe_2 layer induces out-of-plane polarization of the injected spins. However, despite these promising developments, the spin parameters achieved so far are still lower than those obtained with conventional contacts, underscoring the need for further improvements in interface quality.

Forming heterostructures from 2D materials can induce new functionalities, such as spin anisotropy, which could enable the realization of multi-functional spin devices. Spin anisotropy is quantified by the ratio $\xi = \tau_{s,\perp}/\tau_{s,\parallel}$, where $\tau_{s,\perp}$ and $\tau_{s,\parallel}$ represent the spin lifetimes perpendicular and parallel to the material plane, respectively. The oblique Hanle effect is a reliable technique for studying spin transport anisotropy in non-magnetic materials[60]. While spin transport in graphene on conventional SiO_2 substrates is isotropic[60], significant spin anisotropy has been observed in monolayer graphene on transition metal dichalcogenide (TMDC) layers, which favors out-of-plane spin directions[22,61]. This opens avenues for efficient spin manipulation in NLSV devices through precise interface engineering. By combining graphene with TMDCs such as MoS_2[62], or with topological insulators like Bi_2Se_3[63] and $Bi_{1.5}Sb_{0.5}Te_{1.7}Se_{1.3}$[64], proximity SOC can be introduced into graphene, thereby tuning its spin texture and spin anisotropy[65–67]. The anisotropy research has also extended to bilayer
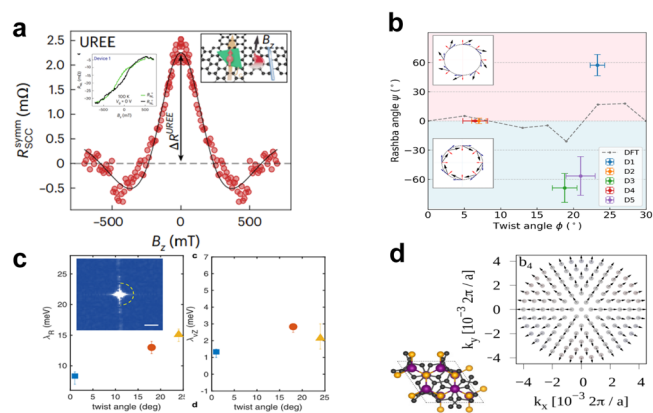
Fig. 5 | Twist engineering of spin texture in graphene based heterostructures.
a Symmetric components of the Hanle spin precession signals of the WSe_2/graphene non-local spin valve device under the perpendicular magnetic field. **b** Rashba angle ψ as a function of twist angle. **c** Fourier transform of quasiparticle interference images of SOC strength of WSe_2/graphene heterostructures with a 30° twist angle. **d** Side view of WSe_2-encapsulated twisted BLG and the calculated spin texture in momentum space. **a**, **b** Reprinted with permission from ref. 77. **c** Reprinted with permission from ref. 78. Copyright 2023 Springer Nature. **d** Reprinted with permission from ref. 79. Copyright 2024 American Physical Society.

graphene encapsulated in hBN dielectrics under applied perpendicular electric fields[68,69]. As illustrated in Fig. 4b, spin lifetime anisotropy in these structures can reach up to 12 at low temperatures[68,69]. Furthermore, the exploration of other vdW materials, such as black phosphorus (BP)[70], has revealed promising spin transport properties. hBN encapsulated BP enables electrical spin manipulation up to RT, with a spin diffusion length exceeding 6 μm and a spin lifetimes of up to 4 ns[70]. Notably, BP exhibits strong anisotropic spin transport[71], as demonstrated by the NLSV measurements in Fig. 4c. These results, supported by oblique Hanle measurements, show a spin lifetime anisotropy greater than 6, with both in-plane and out-of-plane lifetimes on the order of nanoseconds. In contrast to the mentioned graphene-based heterostructures, spin anisotropy in BP is achieved without the need for high SOC substrates. Recent theoretical works suggest that the large spin anisotropy of BP can be dramatically modified by different encapsulations of it with TMDCs[72].

The emerging field of twist engineering introduces an additional degree of freedom for controlling spin textures[73–76]. Theoretical studies have shown that the SOC strength and spin texture modulation in graphene-based heterostructures can be influenced by the twisting angle at the interface[73,74]. This twist angle breaks mirror symmetry, introducing a radial component to the spin texture and leading to unconventional Rashba-Edelstein effects (UREE) and collinear spin-momentum locking[74,76]. Recent work by Yang et al. provides experimental evidence for the manipulation of spin textures and spin-charge conversion in WSe_2/graphene heterostructures through twist angles[77]. Figure 5a illustrates the symmetric components of Hanle spin precession signals in a WSe_2/graphene non-local spin valve device under a perpendicular magnetic field, which are attributed to UREE. Here, the electrically generated non-equilibrium spin density aligns with the applied electric field. Defining the radial component of the spin texture induced by UREE as the Rashba angle ψ, Fig. 5b shows that ψ can be modulated by the twist angle, with both positive and negative radial components oscillating as the twist angle increases. Similarly, C. Renner et al. quantitatively demonstrated through scanning tunnelling microscopy that the strength of SOC in WSe_2/graphene heterostructures can be modulated by crystal twisting[78]. Their results revealed that the proximity SOC consists of a valley-Zeeman term ($\lambda_{vZ} \approx 2$ meV) and a Rashba term ($\lambda_R \approx 15$ meV), as depicted in Fig. 5c. However, this reported Rashba field is significantly stronger than values obtained from DFT simulations and weak localization measurements[15] which typically estimate it to be around 1 meV. The discrepancy may arise from differences in sample quality, measurement conditions and

techniques, highlighting the need for further comparative studies. Moreover, the manipulation of radial Rashba SOC and spin textures in graphene-based heterostructures through twist angles has been extended to more complex twisted multilayer systems, such as WSe_2-encapsulated twisted BLG[79]. As illustrated in the left panel of Fig. 5d, a twist angle of 21.79° was applied to the twisted BLG, with the bottom layer twisted by 20.11° relative to the adjacent WSe_2. The spin texture shown in the right panel of Fig. 5d indicates that the weak Rashba coupling of BLG was enhanced up to 1 meV through twisting, reaching the range required for spin transport experiments, with purely radial spin polarization appearing in the plane parallel to the momentum.

Spin-orbit torques

The efficient manipulation of the magnetization state in magnetic nanostructures using electrical methods has been a central theme in spintronics[12]. Since the observation that an in-plane charge current in heavy metal (HM) thin films can effectively alter the magnetization state of a neighboring FM layer[80], SOT has emerged as a potent and versatile technique for manipulating diverse magnetic materials, ranging from metals to semiconductors and insulators. SOTs are exerted when angular momenta are transferred from spin accumulations generated by various spin-orbit effects, including spin Hall effects[81], Rashba-Edelstein effects[82], and topological surface states[83]. According to the different interactions between spin currents and magnetic moments, SOTs are mainly divided into two types: damping-like torques and field-like torques. The damping-like torques arise from absorbing transverse spin current components with respect to M, given by $\tau_{DL} \sim M \times (M \times \sigma)$, where σ represents spin polarization; while the field-like torques arise from the reflection of the spin current with spin rotation, given by $\tau_{FL} \sim M \times \sigma$. Damping-like torques are more commonly discussed because of their role in exciting the magnetization dynamics. In contrast, field-like torques only destabilize the magnetization when the field-like effective field exceeds the anisotropy field[84].

When the spin Hall effects serve as the spin current source for damping-like torques, as is normally the case for HM/FM or topological insulator (TI)/FM architectures, the damping-like SOT efficiency per unit current density is given by

$$\xi_{DL}^j = T_{int}\theta_{SH}. \tag{1}$$

Here T_{int} represents spin transparency, mediated by two interface-related mechanisms: spin memory loss and spin backflow, generated during the diffusion of spins into the FM layer[85]; θ_{SH} is the spin Hall angle of the spin generator, defined as $\theta_{SH} = (2e/\hbar)j_s/j_c$, evaluating its charge-to-spin conversion[80]. According to Eq. (1), the key to enhancing the effective SOT efficiency in magnetic heterostructures lies in improving the charge-to-spin conversion of the spin generator as well as optimizing the interfacial quality to increase the interfacial spin transparency[86].

Compared with widely investigated HM/FM heterostructures, vdW bilayers offer ideal interfaces with fewer chemical reactions, crystal defects, deposition damage, local strain, and interface dipoles. Therefore, an optimized vdW interface is anticipated to enhance the interfacial spin transparency. Additionally, 2D materials present a rich library of options with significant SOC, magnetism, and tunable spin textures, enabling highly efficient and field-free SOT switching[12].

To create atomically smooth vdW interfaces, the FM layer in the traditional HM/FM architecture was initially substituted with vdW magnet[87]. Through the transfer of exfoliated Fe_3GeTe_2 onto deposited Pt, a vdW heterostructure with an atomically smooth interface was established. In this system, deterministic SOT switching assisted by an in-plane magnetic field was achieved at 120 K, displaying a SOT critical current density (j_{sw}) of 1.2×10^7 A cm^{-2}. The damping-like SOT efficiency ξ_{DL}^j, extracted from second harmonic measurements, was observed to be 0.12, consistent with previously reported values for Pt[87]. Furthermore, the vdW semimetal WTe_2 and ferromagnet Fe_3GeTe_2 are utilized to meet the requirements of an all-vdW heterostructure with an
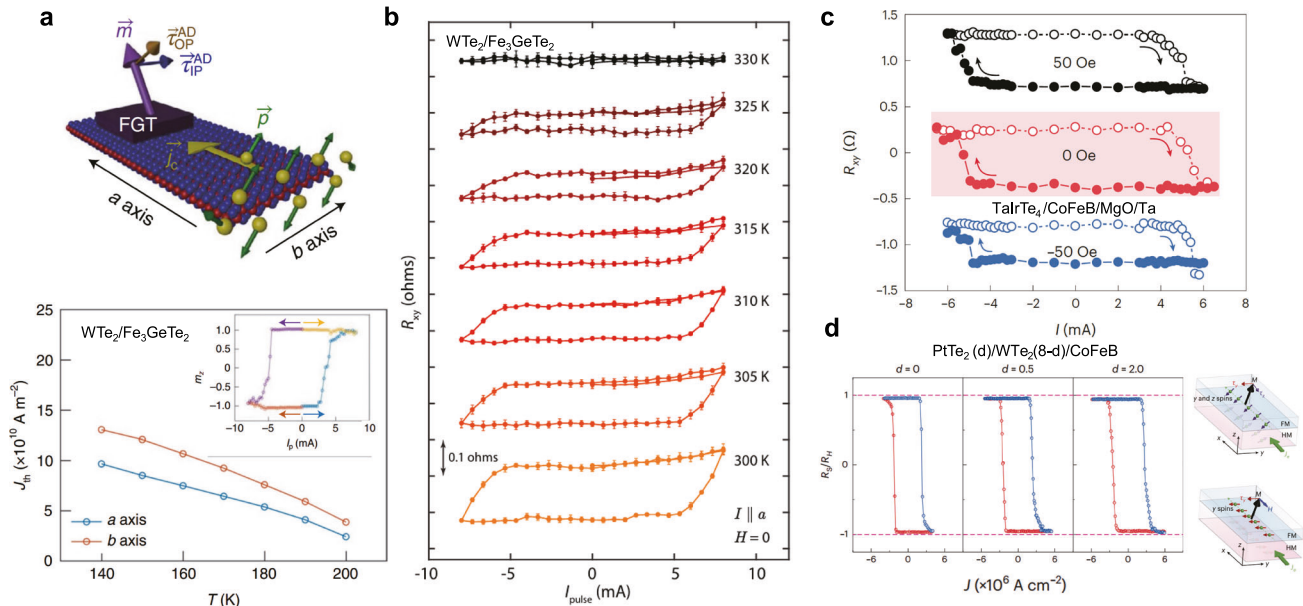
Fig. 6 | Spin-orbit torques in van der Waals heterostructures. a top panel illustrates the forms of damping-like spin torque in all-vdW WTe$_2$/Fe$_3$GeTe$_2$ heterostructure. When a charge current is applied along the a-axis of WTe$_2$, the spin polarization of electrons has an out-of-plane component, as indicated by green arrows. The bottom panel illustrates the SOT critical current density of the WTe$_2$/Fe$_3$GeTe$_2$ heterostructure when current is applied along the a-axis and b-axis at different temperatures. The inset shows the field-free SOT switching achieved by applying current along the a-axis at 160 K. **b** A series of field-free SOT switching loops at various temperature above 300 K in WTe$_2$/Fe$_3$GaTe$_2$ heterostructure.

c Current-induced magnetization switching in TaIrTe$_4$/Ti/CoFeB/MgO/Ta heterostructure in the presence external magnetic fields along the x axis of −50 Oe (blue), 0 Oe (red) and 50 Oe (black). **d** Schematic diagram of SOT device based on perpendicular magnetic anisotropic HM/FM structure, and current driven magnetic switching in PtTe$_2$ (d)/WTe$_2$ (8 − d)/CoFeB heterostructures. **a** Reprinted with permission from ref. 89. Copyright 2022 Springer Nature **b**, Reprinted with permission from ref. 96. Copyright 2024 AAAS. **c** Reprinted with permission from ref. 90. Copyright 2023 Springer Nature. **d** Reprinted with permission from ref. 99. Copyright 2024 Springer Nature.

atomically sharp interface. The field-assisted SOT deterministic switching has been reported in these structures[23]. Compared to Pt/Fe$_3$GeTe$_2$, the interface quality of WTe$_2$/Fe$_3$GeTe$_2$ has been significantly improved. Additionally, due to the larger spin Hall angle of WTe$_2$, measured as 4.6, j_{sw} has been reduced by an order of magnitude to the minimum value of 3.9×10^6 A cm^{-2} below 200 K.

Besides optimizing the interface quality to reduce spin loss, which can be achieved through vdW interfaces, another prominent topic in SOT is field-free switching. Normally, due to the x-z symmetry protection in a HM/FM heterostructure, a fixed current direction cannot access a unique magnetization direction. To achieve deterministic SOT switching, an in-plane magnetic field is required to break the x-z symmetry[88]. In recent years, to better meet practical application needs, efforts have been made to realize field-free SOT switching by leveraging the materials with non-trivial symmetry. In the library of van der Waals materials, WTe$_2$[89] and TaIrTe$_4$[90–92] are promising materials that support field-free SOT switching.

The space group of bulk WTe$_2$ crystals is $Pmn2_1$[93]. In the WTe$_2$/FM bilayer, the helical axis symmetry and glide plane symmetry of this space group are broken at the interface. As a result, the WTe$_2$/FM bilayer only retains mirror symmetry with respect to the b-c plane; there is no mirror symmetry in the a-c plane. Consequently, there is no 180° rotational symmetry about the c-axis. When a current is applied along the bilayer's low symmetry axis, an out-of-plane damping-like SOT is anticipated[93]. As shown in the top panel of Fig. 6a, by applying current along the low symmetry axis of WTe$_2$, field-free SOT switching has been achieved in the all-vdW WTe$_2$/Fe$_3$GeTe$_2$ heterostructure at temperatures below 200 K[89]. The bottom panel of Fig. 6a depicts the temperature dependence of j_{sw} in WTe$_2$/Fe$_3$GeTe$_2$ heterostructure. When the temperature increases from 140 K to 200 K, j_{sw} for both a and b axes decrease, reaching the minimum value of 9.8×10^{10} A cm^{-2} at 200 K. Notably, when the current is applied along the axis a with lower symmetry, the current density would be smaller. Despite achieving field-free SOT switching for the first time through the intrinsic crystal symmetry breaking of the vdW interface, which is absent in

traditional HM/FM heterostructures, e.g., Pt/Co and Ta/CoFeB/MgO system, the magnitude of j_{sw} up to 10^{10} A cm^{-2} level and the operating temperature lower than 200 K was limiting the application of all-vdW WTe$_2$/Fe$_{2.78}$GeTe$_2$ on SOT-MRAM.

Similarly, the Type-II Weyl semi-metal TMDC material TaIrTe$_4$, which belongs to the Pmn2$_1$ space group and possesses a broken two-fold rotational symmetry, has attracted interest due to its unique spin textures and sizable out-of-plane damping-like SOT efficiency[90,91]. Utilizing bilinear magnetoelectric resistance and spin-torque ferromagnetic resonance measurements, the out-of-plane tilting angle of spin in TaIrTe$_4$ has been determined to be 8 degrees[90]. RT field-free SOT switching in TaIrTe$_4$/CoFeB heterostructure has been achieved, with the out-of-plane spin Hall conductivity evaluated as 5.44×10^4 ($\hbar / 2e$) $(\Omega m)^{-1}$ [90], as shown in Fig. 6c. Similarly, in TaIrTe$_4$/Ni$_{80}$Fe$_{20}$ heterostructure, the RT out-of-plane spin Hall conductivity is reported as $(4.05 \pm 0.23) \times 10^4$ ($\hbar/2e$) $(\Omega m)^{-1}$, an order of magnitude higher than the reported values in other materials[91]. Theoretical calculations indicate that the out-of-plane spin polarization is forbidden for the bulk material with Pmn2$_1$ space group[94], therefore, for TaIrTe$_4$, the out-of-plane polarized spin currents mainly originate from the surface[92]. These findings highlight the potential of atomically smooth vdW interfaces in enhancing unconventional SOT efficiency in TaIrTe$_4$-based systems. Recent studies have demonstrated that vdW heterostructures, such as TaIrTe$_4$/Fe$_3$GaTe$_2$, can enable energy-efficient, field-free SOT switching with significantly reduced current and power densities, achieving better performance than conventional systems[92,95].

In order to realize the RT magnetic switching in vdW heterostructures, efforts have focused on enhancing T_c of 2D magnets through interface engineering. For example, the interfacial exchange coupling between epitaxial-grown Bi$_2$Te$_3$ and Fe$_3$GeTe$_2$ has been demonstrated to enhance the T_c of Fe$_3$GeTe$_2$[21]. The interface quality has been optimized in this system and the intrinsic T_c of Fe$_3$GeTe$_2$ increases from 210 K to 400 K after epitaxial growth on Bi$_2$Te$_3$. Additionally, optimized interface quality also provides larger spin transparency, resulting in a highly efficient SOT switching in

Bi_2Te_3/Fe_3GeTe_2 heterostructure. Similarly, with optimized interface quality, Kajale et al., have realized the RT field-free SOT switching in Fe_3GeTe_2/WTe_2 heterostructure[96]. The operating temperature is enhanced to 320 K, and the minimum value of j_{sw} is reported as 2.23×10^{10} A cm^{-2}, as shown in Fig. 6b.

In addition to investigating TMDCs with unique symmetries for unconventional SOT switching, combining the emerging noble TMDC materials for example $PtSe_2$[97] and $PtTe_2$[98], with sizable SOC and the widely studied WTe_2, which breaks inversion symmetry, enables highly efficient charge-to-spin conversion in unconventional field-free SOT switching[99], as illustrated in the right panel of Fig. 6d. In this context, $PtTe_2$ exhibits a large y-spin Hall conductivity $\sigma_{s,y} \approx 2.32 \times 10^5 \times \hbar/2e$ Ω^{-1} m^{-1}, and WTe_2 has a z-spin Hall conductivity $\sigma_{s,z} \approx 0.25 \times 10^5 \times \hbar/2e$ Ω^{-1} m^{-1}. When current is injected from the bottom $PtTe_2$, the in-plane spins of $PtTe_2$ generated by the spin Hall effect are transformed into out-of-plane spins through the crystal symmetry breaking of WTe_2. Thereby, the field-free SOT switching driven by unconventional out-of-plane spins in CoFeB is achieved[99]. As shown in the left panel of Fig. 6d, as the thickness of WTe_2 decreases, j_c of field-free SOT switching decreases accordingly, accompanied by the disappearance of the switching loop, indicating that the crystal asymmetry of WTe_2 leads to the conversion of in-plane spins from $PtTe_2$ to out-of-plane spins. The linear response theory suggests that the intrinsic symmetry breaking in WTe_2 leads to non-zero response tensors of spin accumulation in the z-direction to the spin current in the y-direction, thereby introducing out-of-plane spins and the corresponding spin torques.

Lastly, it is important to mention that recent studies have explored the thickness dependence of spin-orbit torques in vdW materials, revealing distinct charge-to-spin conversion mechanisms at different thicknesses. For instance, in monolayer to trilayer $PtSe_2$, the dominant spin generation mechanism is the REE, while in thicker layers (>3 nm), the spin Hall effect SHE becomes dominant[97]. Similarly, WTe_2 monolayers exhibit robust out-of-plane antidamping torques despite the absence of conventional spin Hall currents, making them promising candidates for field-free switching applications[100]. Furthermore, given the minimal sub-ns time scale of SOT switching[101], and the lowest critical current density, 0.52×10^{-6} A/m^{-2} in $(BiSb)_2Te_3$[102], exploring the road map to further enhance the performance of SOT device by utilizing vdW interfaces will be intriguing topics.

In conclusion, based on the traditional HM/FM architecture, vdW materials provide atomically smooth interfaces, thereby enhancing interface spin transparency. Meanwhile, optimized interfaces enhance interfacial exchange coupling, which boosts the Curie temperature of 2D ferromagnets and enables RT field-free SOT switching in all-vdW structures. Additionally, the rich library of vdW materials allows for the use of materials with larger SOC as spin generators, thereby achieving greater damping-like SOT efficiency.

Quantum spintronics

To achieve energy-efficient spintronic devices, exploration is underway into quantum materials as a new frontier. Moiré superlattice is one of the emerging candidates, formed when two vdW layers are stacked together. With the presence of twist angle θ and lattice mismatch δ, the Moiré period a_M is derived as $a_M = a/\sqrt{\delta^2 + \theta^2}$, where a represents the lattice constant of vdW layer. Since the Moiré period a_M is always greater than the vdW lattice constant a, low-energy physics (mediated by a_M) and high-energy physics (mediated by a) could be separated within the Moiré superlattice. Therefore, electrons can be considered to move in a smooth periodic potential, and Bloch's theorem applies to the mini-Brillouin zone associated with the Moiré superlattice resulting in Moiré flat bands[103]. The emergence of Moiré length scale a_M also enables Moiré superlattice a unique platform for investigating the strong correlation physics[104]. For the same site in a Moiré superlattice, the kinetic energy of the electrons scales as a_M^{-2}, while the Coulomb interaction between electrons scales as $a_M^{-1/2}$, indicating Coulomb interaction dominates over kinetic energy for large Moiré length scale[105]. Consequently, strong correlations among electrons are induced, accompanied by a series of novel quantum phases, including superconductivity[106] and the fractional quantum spin Hall effect[107].

Importantly, Berry curvature plays a fundamental role in electronic transport, particularly in moiré superlattices where symmetry breaking can lead to topological effects. Moiré systems provide a tunable platform for engineering Berry curvature hotspots, which influence spin-charge conversion, anomalous transport, and valley Hall effects. For instance, in twisted bilayer graphene[108] and $MoTe_2$/WSe_2[109] heterostructures, symmetry engineering modifies the band topology, leading to nontrivial spin and valley-dependent transport phenomena. The interplay between Berry curvature and correlation effects in these systems has also enabled the realization of exotic states such as quantum anomalous Hall and nonlinear Hall effects. A recent review provides an extensive discussion of Berry physics in moiré materials, and readers interested in further details may refer to ref. 110.

Moiré superlattice provides a wide range of novel spin-orbit effects, including topological insulating states[111] and ferromagnetism[29], enabling more efficient spin manipulating. One fascinating material is Moiré superlattice—based Chern insulator. According to the Hubbard model, simultaneously tuning electron hopping and SOC strength by twisting makes it possible to open the gap of flat bands while breaking the time-reversal symmetry of the band structure[112], as shown in Fig. 7a. This can transform the material into a Chern insulator with both high Berry curvature and ferromagnetism, where giant spin Hall effect and SOT switching in nanoampere level are expected.

Beyond theoretical predictions, in t-BLG with a twist angle of 1.17° aligned with hBN, a ferromagnetic state was experimentally introduced by utilizing enhanced electron-electron interactions in the nearly three-quarters filled conduction band for the first time[29]. Here, the charge density n is independently tuned by the perpendicular displacement field. Within the n range corresponding to the insulating state, ferromagnetic hysteresis, giant anomalous Hall effect of 10.4 kΩ, and chiral edge states are observed, indicating that the system is an incipient Chern insulator. Furthermore, the magnetization of the sample is observed to be switched by a small current of ~50 nA, paving the way of Moiré materials in spintronic applications. Next, Serlin et al. observed the quantum anomalous Hall effect induced by intrinsic strong electron-electron interactions in t-BLG (with a twist angle of $1.15 \pm 0.01°$) aligned with hBN[30]. As shown in Fig. 7b, with filling factor $\nu = 3$ and temperature of 1.6 K, the response of the Hall resistance R_{xy} to the magnetic field was measured for different charge densities. The Hall resistance exhibits hysteresis with a coercivity of several tens of milli-tesla. Around the charge density $n = 2.37 \times 10^{12}$ cm^{-2}, R_{xy} reached a quantized plateau of $\hbar/e^2$. These results indicate that the system's quantum anomalous Hall (QAH) state is stabilized by the spontaneous breaking of time-reversal symmetry. Theoretical calculations elucidate the origin of magnetic order: when an excess valley-polarized and spin-polarized Chern band is occupied, the exchange energy of the system reaches its minimum, spontaneously breaking time-reversal symmetry. Additionally, the weak SOC in graphene provides anisotropy for magnetic order.

Subsequently, Deng et al. also observed the layer-dependent QAH states at 1.4 K in five layers of $MnBi_2Te_4$ thin films with intrinsic magnetism[113], as shown in Fig. 7c. Upon aligning the magnetization of all layers with an external magnetic field, the precisely quantified QAH state was observed up to 6.5 K, surpassing the 1.6 K of the t-BLG/hBN system, as shown in the inset of Fig. 7c. It is noteworthy that the field-free current-driven magnetic switching with the critical current of a few nA levels has been observed in t-BLG/hBN QAH insulators[29,30]. Beyond the widely investigated HM/FM architecture, low-energy electrically modulated magnetic switching can also be achieved using QAH insulators. Therefore, the current-driven magnetic switching in magnetic Chern insulators and elucidating their physical mechanisms became a subject of interest.
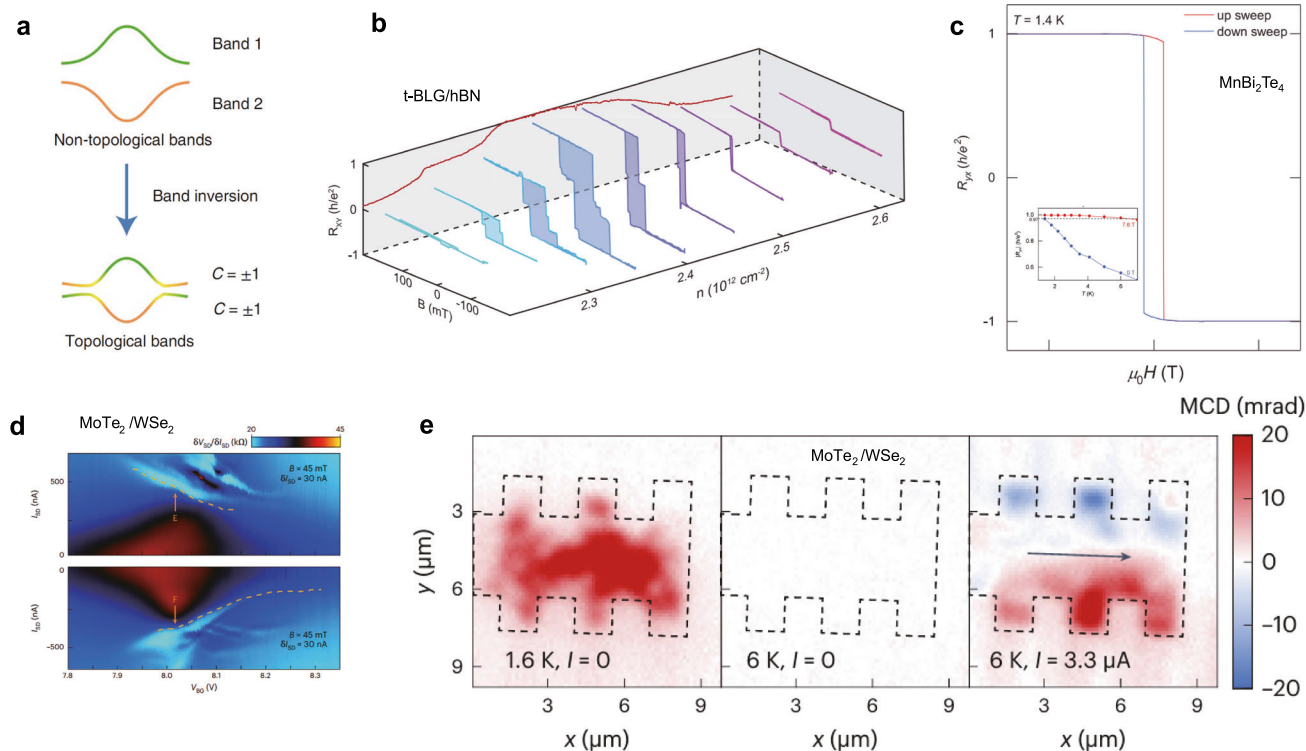
Fig. 7 | Quantum spintronics in Moiré heterostructures. a Schematic illustration of the intertwined two Moiré flat bands through band inversion and interlayer hybridization. After band inversion, these bands acquire finite valley-resolved Chern numbers, thus becoming topological bands. **b** Hall resistance R_{xy} of t-BLG aligned with hBN, plotted as a function of magnetic field and carrier density. **c** QAH states for 5-layer $MnBi_2Te_4$ thin film at 1.4 K. The inset figure is R_{xy} plotted as a function of temperature obtained under external magnetic fields of 7.6 T. **d** The differential two-terminal resistance as a function of back gate voltage and and source-drain current in AB-stacked $MoTe_2/WSe_2$ magnetic Chern insulator. **e** MCD images of AB-stacked $MoTe_2/WSe_2$ magnetic Chern insulator taken at the centre of the QAH region at 1.6 K with zero-bias current (left panel), 6 K with zero-bias current (middle panel) and 6 K with a bias current of 3.3 μA. Black dashed lines mark the sample boundaries and arrows show the bias current direction. **a** Reprinted with permission from ref. 112. Copyright 2019 American Physical Society. **b** Reprinted with permission from ref. 30. Copyright 2020 AAAS. **c**, Reprinted with permission from ref. 113. Copyright 2020 AAAS **d**, Reprinted with permission from ref. 114. Copyright 2023 Springer Nature. **e** Reprinted with permission from ref. 109. Copyright 2024 Springer Nature.

For instance, as shown in Fig. 7d, magnetic imaging shows the current switching of single magnetic domains in AB-stacked $MoTe_2/WSe_2$ magnetic Chern insulator, indicating the role of intrinsic spin or valley Hall torques of current-driven magnetic switching in quantum moiré material systems[114].

Recently, utilizing direct magneto-optical imaging, sizable intrinsic spin Hall effect and ferromagnetism have been observed to coexist in AB-stacked $MoTe_2/WSe_2$ Moiré bilayers[109]. Under a current density of less than 1 A m^{-1}, spin accumulation towards the lateral edges of the sample has been observed, approaching the near-saturation spin density, as shown in Fig. 7e. This result demonstrates the long-range spin Hall transport and effective non-local spin accumulation in Moiré heterostructures.

Emerging studies on the magnetic order and spin Hall effect in vdW QAH insulators have provided a clear pathway for the future development of spintronics: the novel quantum material system can be utilized to achieve bulk energy-efficient, current-driven magnetic switching. Recently, in rhombohedral Gr/WS$_2$ Moiré heterostructures, the QAH state of graphene has been further enhanced through the combined effects of electron correlation and proximity-induced Ising SOC[115]. This result indicates that TMDC materials with larger SOC strength can further stabilize the QAH state.

Conclusion & Outlook

Since magnetism was observed in ultrathin CrI$_3$[116] and Cr$_2$GeTe$_2$[117], vdW heterostructures-based devices have been intensively investigated to manipulate the spin degrees of freedom. The subsequent focus has been on vdW heterostructures with atomically smooth interfaces, which not only allow efficient spin transport but also serve as platforms for extending spin-orbit effects, including exchange bias, proximity-induced ferromagnetism, spin-lifetime anisotropy, gate voltage-tunable spin polarization, higher spin transparency, and unconventional SOTs. In recent years, the emerging moiré engineering has brought unexpected novel spintronic effects to vdW interfaces, such as twist-angle tunable SOC and Chern magnetic states with nanoampere-level current-driven magnetization switching[118].

Nevertheless, research on spin-orbit effects at vdW interfaces is still in its early stages; the emerging interfacial twist engineering can bring new opportunities for spintronics. In addition to the manipulation of SOC, spin texture, and topologically non-trivial states mentioned in this review indicate the potential to achieve complex magnetic ground states and modulate exchange interactions in twisted vdW ferromagnets. Therefore, the emerging twist engineering has the potential to reshape vdW spintronics from various aspects, offering new, efficient, and low-energy solutions for future low-power electronic devices.

References
1. Dieny, B. et al. Opportunities and challenges for spintronics in the microelectronics industry. *Nat. Electron.* **3**, 446–459 (2020).
2. Manipatruni, S., Nikonov, D. E. & Young, I. A. Beyond CMOS computing with spin and polarization. *Nat. Phys.* **14**, 338–343 (2018).
3. Esch, J. Overview of beyond-CMOS devices and a uniform methodology for their benchmarking. *Proc. IEEE* **101**, 2495–2497 (2013).

4. Žutić, I., Fabian, J. & Sarma, S. D. Spintronics: Fundamentals and applications. *Rev. Mod. Phys.* **76**, 323 (2004).
5. Novoselov, K. S. et al. Electric field effect in atomically thin carbon films. *Science* **306**, 666–669 (2004).
6. Manzeli, S., Ovchinnikov, D., Pasquier, D., Yazyev, O. V. & Kis, A. 2D transition metal dichalcogenides. *Nat. Rev. Mater.* **2**, 17033 (2017).
7. Novoselov, K. S. et al. Two-dimensional atomic crystals. *PNAS* **102**, 10451–10453 (2005).
8. Radisavljevic, B., Radenovic, A., Brivio, J., Giacometti, V. & Kis, A. Single-layer MoS_2 transistors. *Nat. Nanotechnol.* **6**, 147–150 (2011).
9. Novoselov, K. S., Mishchenko, A., Carvalho, A. & Neto, A. H. C. 2D materials and van der Waals heterostructures. *Science* **353**, aac9439 (2016).
10. Avsar, A. et al. Colloquium: Spintronics in graphene and other two-dimensional materials. *Rev. Mod. Phys.* **92**, 021003 (2020).
11. Sierra, J. F., Fabian, J., Kawakami, R. K., Roche, S. & Valenzuela, S. O. Van der Waals heterostructures for spintronics and opto-spintronics. *Nat. Nanotechnol.* **16**, 856–868 (2021).
12. Yang, H. et al. Two-dimensional materials prospects for non-volatile spintronic memories. *Nature* **606**, 663–673 (2022).
13. Dayen, J.-F., Ray, S. J., Karis, O., Vera-Marun, I. J. & Kamalakar, M. V. Two-dimensional van der Waals spinterfaces and magnetic-interfaces. *Appl. Phys. Rev.* **7**, 011303 (2020).
14. Perkins, D. T. S. & Ferreira, A. Spintronics in 2D graphene-based van der Waals heterostructures. In: *Encyclopedia of Condensed Matter Physics*) (2024).
15. Garcia, J. H., Vila, M., Cummings, A. W. & Roche, S. Spin transport in graphene/transition metal dichalcogenide heterostructures. *Chem. Soc. Rev.* **47**, 3359–3379 (2018).
16. Žutić, I., Matos-Abiague, A., Scharf, B., Dery, H. & Belashchenko, K. Proximitized materials. *Mater. Today* **22**, 85–107 (2019).
17. Wang, Y. & Chhowalla, M. Making clean electrical contacts on 2D transition metal dichalcogenides. *Nat. Rev. Phys.* **4**, 101–112 (2021).
18. Ghiasi, T. S. et al. Electrical and thermal generation of spin currents by magnetic bilayer graphene. *Nat. Nanotechnol.* **16**, 788–794 (2021).
19. Fülöp, B. et al. Boosting proximity spin–orbit coupling in graphene/WSe_2 heterostructures via hydrostatic pressure. *npj 2D Mater. Appl.* **5**, 82 (2021).
20. Huang, X. et al. Manipulating exchange bias in 2D magnetic heterojunction for high-performance robust memory applications. *Nat. Commun.* **14**, 2190 (2023).
21. Wang, H. et al. Room temperature energy-efficient spin-orbit torque switching in two-dimensional van der Waals Fe_3GeTe_2 induced by topological insulators. *Nat. Commun.* **14**, 5173 (2023).
22. Ghiasi, T. S., Ingla-Aynés, J., Kaverzin, A. A. & Wees, B. J. v. Large proximity-induced spin lifetime anisotropy in transition-metal dichalcogenide/graphene heterostructures. *Nano Lett.* 17, 7528–7532 (2017).
23. Shin, I. et al. Spin-Orbit Torque Switching in an All-Van der Waals Heterostructure. *Adv. Mater.* **34**, e2101730 (2022).
24. Tang, W., Liu, H., Li, Z., Pan, A. & Zeng, Y.-J. Spin-Orbit Torque in Van der Waals-Layered Materials and Heterostructures. *Adv. Sci.* **8**, e2100847 (2021).
25. Sharpe, A. L. et al. Emergent ferromagnetism nearthree-quarters filling in twistedbilayer graphene. *Science* **365**, 605–608 (2019).
26. Kennes, D. M. et al. Moiré heterostructures as a condensed-matter quantum simulator. *Nat. Phys.* **17**, 155–163 (2021).
27. Cao, Y. et al. Unconventional superconductivity in magic-angle graphene superlattices. *Nature* **556**, 43–50 (2018).
28. Zhang, Y. et al. Enhanced superconductivity in spin-orbit proximitized bilayer graphene. *Nature* **613**, 268–273 (2023).
29. Sharpe, A. L. et al. Emergent ferromagnetism near three-quarters filling in twisted bilayer graphene. *Science* **365**, 605 (2019).
30. Serlin, M. et al. Intrinsic quantized anomalous Hall effect in a moiré heterostructure. *Science* **367**, 900 (2020).
31. Karpiak, B. et al. Magnetic proximity in a van der Waals heterostructure of magnetic insulator and graphene. *2D Mater.* **7**, 015026 (2020).
32. Wang, W. et al. Clean assembly of van der Waals heterostructures using silicon nitride membranes. *Nat. Electron.* **6**, 981–990 (2023).
33. Purdie, D. G. et al. Cleaning interfaces in layered materials heterostructures. *Nat. Commun.* **9**, 5387 (2018).
34. Parkin, S. S. et al. Giant tunnelling magnetoresistance at room temperature with MgO (100) tunnel barriers. *Nat. Mater.* **3**, 862–867 (2004).
35. Safranski, C., Hu, G., Hashemi, P. & Brown, S. L. Reliable sub-nanosecond MRAM with double spin-torque magnetic tunnel junctions. In: *IEEE Symposium on VLSI Technology and Circuits (VLSI Technology and Circuits)* (2022).
36. Deng, Y. et al. Gate-tunable room-temperature ferromagnetism in two-dimensional Fe_3GeTe_2. *Nature* **563**, 94–99 (2018).
37. Wang, Z. et al. Tunneling spin valves based on Fe_3GeTe_2/hBN/Fe_3GeTe_2 van der Waals heterostructures. *Nano Lett.* **18**, 4303–4308 (2018).
38. Min, K. H. et al. Tunable spin injection and detection across a van der Waals interface. *Nat. Mater.* **21**, 1144–1149 (2022).
39. Zhu, W. et al. Large and tunable magnetoresistance in van der Waals ferromagnet/semiconductor junctions. *Nat. Commun.* **14**, 5371 (2023).
40. Zhang, S. & Levy, P. M. Quenching of magnetoresistance by hot electrons in magnetic tunnel junctions. *Phys. Rev. Lett.* **79**, 3744 (1997).
41. Zhang, S. Spin Hall effect in the presence of spin diffusion. *Phys. Rev. Lett.* **85**, 393 (2000).
42. Tsymbal, E. Y. & Pettifor, D. G. The influence of impurities within the barrier on tunneling magnetoresistance. *J. Appl. Phys.* **85**, 5801–5803 (1999).
43. Zhu, W. et al. Large room-temperature magnetoresistance in van der Waals ferromagnet/semiconductor junctions. *Chin. Phys. Lett.* **39**, 128501 (2022).
44. Chen, X. et al. Octupole-driven magnetoresistance in an antiferromagnetic tunnel junction. *Nature* **613**, 490–495 (2023).
45. Qin, P. et al. Room-temperature magnetoresistance in an all-antiferromagnetic tunnel junction. *Nature* **613**, 485–489 (2023).
46. Telford, E. J. et al. Coupling between magnetic order and charge transport in a two-dimensional magnetic semiconductor. *Nat. Mater.* **21**, 754–760 (2022).
47. Boix-Constant, C. et al. Multistep magnetization switching in orthogonally twisted ferromagnetic monolayers. *Nat. Mater.* **23**, 212–218 (2024).
48. Chen, Y. et al. Twist-assisted all-antiferromagnetic tunnel junction in the atomic limit. *Nature* **632**, 1045–1051 (2024).
49. Xu, Y. et al. Coexisting ferromagnetic antiferromagnetic state in twisted bilayer CrI_3. *Nat. Nanotechnol.* **17**, 143–147 (2022).
50. Grollier, J. et al. Neuromorphic spintronics. *Nat. Electron.* **3**, 360–370 (2020).
51. Borders, W. A. et al. Integer factorization using stochastic magnetic tunnel junctions. *Nature* **573**, 390–393 (2019).
52. Nguyen, L.-A. T. et al. Electrically tunable magnetic fluctuations in multilayered vanadium-doped tungsten diselenide. *Nat. Electron.* **6**, 582–589 (2023).
53. BehinAein, B., Datta, D., Salahuddin, S. & Datta, S. Proposal for an all-spin logic device with built-in memory. *Nat. Nanotechnol.* **5**, 266–270 (2010).
54. Kamalakar, M. V., Groenveld, C., Dankert, A. & Dash, S. P. Long distance spin communication in chemical vapour deposited graphene. *Nat. Commun.* **6**, 6766 (2015).
55. Khokhriakov, D. et al. Multifunctional spin logic operations in graphene spin circuits. *Phys. Rev. Appl.* **18**, 064063 (2022).

56. Khokhriakov, D., Karpiak, B., Hoque, M. D. A. & Dash, S. P. Two-dimensional spintronic circuit architectures on large scale graphene. *Carbon* **161**, 892–899 (2020).

57. Drogeler, M. et al. Spin lifetimes exceeding 12 ns in graphene nonlocal spin valve devices. *Nano Lett.* **16**, 3533–3539 (2016).

58. Zhao, B. et al. A room-temperature spin-valve with van der Waals ferromagnet Fe_5GeTe_2/graphene heterostructure. *Adv. Mater.* **35**, e2209113 (2023).

59. Pan, H. et al. Room-Temperature Lateral Spin Valve in Graphene/Fe_3GaTe_2 van der Waals heterostructures. *ACS Mater. Lett.* **5**, 2226–2232 (2023).

60. Raes, B. et al. Determination of the spin-lifetime anisotropy in graphene using oblique spin precession. *Nat. Commun.* **7**, 11444 (2016).

61. Benítez, L. A. et al. Strongly anisotropic spin relaxation in graphene–transition metal dichalcogenide heterostructures at room temperature. *Nat. Phys.* **14**, 303–308 (2017).

62. Hoque, M. D. A. et al. Spin-valley coupling and spin-relaxation anisotropy in all-CVD Graphene-MoS_2 van der Waals heterostructure. *Phys. Rev. Mater.* **7**, 044005 (2023).

63. Khokhriakov, D. et al. Tailoring emergent spin phenomena in Diracmaterial heterostructures. *Sci. Adv.* **4**, eaat9349 (2018).

64. Hoque, M. D. A., Sjöström, L., Khokhriakov, D., Zhao, B. & Dash, S. P. Room temperature nonlocal detection of charge-spin interconversion in a topological insulator. *npj 2D Mater. Appl.* **8**, 10 (2024).

65. Avsar, A. et al. Spin-orbit proximity effect in graphene. *Nat. Commun.* **5**, 4875 (2014).

66. Wang, Z. et al. Strong interface-induced spin-orbit interaction in graphene on WS_2. *Nat. Commun.* **6**, 8339 (2015).

67. Benitez, L. A. et al. Tunable room-temperature spin galvanic and spin Hall effects in van der Waals heterostructures. *Nat. Mater.* **19**, 170–175 (2020).

68. Leutenantsmeyer, J. C., Ingla-Aynés, J., Fabian, J. & van Wees, B. J. Observation of spin-valley-coupling-induced large spin-lifetime anisotropy in bilayer graphene. *Phys. Rev. Lett.* **121**, 127702 (2018).

69. Xu, J., Zhu, T., Luo, Y. K., Lu, Y. M. & Kawakami, R. K. Strong and tunable spin-lifetime anisotropy in dual-gated bilayer graphene. *Phys. Rev. Lett.* **121**, 127703 (2018).

70. Avsar, A. et al. Gate-tunable black phosphorus spin valve with nanosecond spin lifetimes. *Nat. Phys.* **13**, 888–893 (2017).

71. Cording, L. et al. Highly anisotropic spin transport in ultrathin black phosphorus. *Nat. Mater.* **23**, 479–485 (2024).

72. Milivojević, M., Gmitra, M., Kurpas, M., Štich, I. & Fabian, J. Proximity-enabled control of spin-orbit coupling in phosphorene symmetrically and asymmetrically encapsulated by WSe_2 monolayers. *Phys. Rev. B* **109**, 075305 (2024).

73. Li, Y. & Koshino, M. Twist-angle dependence of the proximity spin-orbit coupling in graphene on transition-metal dichalcogenides. *Phys. Rev. B* **99**, 075438 (2019).

74. Lee, S. et al. Charge-to-spin conversion in twisted graphene/WSe_2 heterostructures. *Phys. Rev. B* **106**, 165420 (2022).

75. Péterfalvi, C. G., David, A., Rakyta, P., Burkard, G. & Kormányo, A. Quantum interference tuning of spin-orbit coupling in twisted van der Waals trilayers. *Phys. Rev. Res.* **4**, L022049 (2022).

76. Veneri, A., Perkins, D. T. S., Péterfalvi, C. G. & Ferreira, A. Twist angle controlled collinear Edelstein effect in van der Waals heterostructures. *Phys. Rev. B* **106**, L081406 (2022).

77. Yang, H. et al. Twist-angle-tunable spin texture in WSe_2/graphene van der Waals heterostructures. *Nat. Mater.* **23**, 1502–1508 (2024).

78. Sun, L. et al. Determining spin-orbit coupling in graphene by quasiparticle interference imaging. *Nat. Commun.* **14**, 3771 (2023).

79. Frank, T., Junior, P. E. F., Zollner, K. & Fabian, J. Emergence of radial Rashba spin-orbit fields in twisted van der Waals heterostructures. *Phys. Rev. B* **109**, L241403 (2024).

80. Liu, L. et al. Spin-torque switching with the giant spin Hall effect of tantalum. *Science* **336**, 555–558 (2012).

81. Guo, G. Y., Murakami, S., Chen, T. W. & Nagaosa, N. Intrinsic spin Hall effect in platinum: first-principles calculations. *Phys. Rev. Lett.* **100**, 096401 (2008).

82. Shao, Q. et al. Strong Rashba-Edelstein effect-induced spin-orbit torques in monolayer transition metal dichalcogenide/ferromagnet bilayers. *Nano Lett.* **16**, 7514–7520 (2016).

83. Mellnik, A. R. et al. Spin-transfer torque generated by a topological insulator. *Nature* **511**, 449–451 (2014).

84. Aradhya, S. V., Rowlands, G. E., Oh, J., Ralph, D. C. & Buhrman, R. A. Nanosecond-timescale low energy switching of in-plane magnetic tunnel junctions through dynamic oersted-field-assisted spin hall effect. *Nano Lett.* **16**, 5987–5992 (2016).

85. Zhu, L., Ralph, D. C. & Buhrman, R. A. Maximizing spin-orbit torque generated by the spin Hall effect of Pt. *Appl. Phys. Rev.* **8**, 031308 (2021).

86. Gupta, K., Wesselink, R. J. H., Liu, R., Yuan, Z. & Kelly, P. J. Disorder dependence of interface spin memory loss. *Phys. Rev. Lett.* **124**, 087702 (2020).

87. Wang, X. et al. Current-driven magnetization switching in a van derWaals ferromagnet Fe_3GeTe_2. *Sci. Adv.* **5**, eaaw8904 (2019).

88. Yu, G. et al. Switching of perpendicular magnetization by spin-orbit torques in the absence of external magnetic fields. *Nat. Nanotechnol.* **9**, 548–554 (2014).

89. Kao, I. H. et al. Deterministic switching of a perpendicularly polarized magnet using unconventional spin-orbit torques in WTe_2. *Nat. Mater.* **21**, 1029–1034 (2022).

90. Liu, Y. et al. Field-free switching of perpendicular magnetization at room temperature using out-of-plane spins from $TaIrTe_4$. *Nat. Electron.* **6**, 732–738 (2023).

91. Bainsla, L. et al. Large out-of-plane spin-orbit torque in topological Weyl semimetal $TaIrTe_4$. *Nat. Commun.* **15**, 4649 (2024).

92. Zhang, Y. et al. Robust field-free switching using large unconventional spin-orbit torque in an all-Van der Waals heterostructure. *Adv. Mater.* **36**, e2406464 (2024).

93. MacNeill, D. et al. Control of spin–orbit torques through crystal symmetry in WTe2/ferromagnet bilayers. *Nat. Phys.* **13**, 300–305 (2016).

94. Železný, J. et al. Spin-orbit torques in locally and globally noncentrosymmetric crystals: antiferromagnets and ferromagnets. *Phys. Rev. B* **95**, 014403 (2017).

95. Pandey, L. et al. Energy-efficient field-free unconventional spin-orbit torque magnetization switching dynamics in van der Waals heterostructures. Preprint at https://arxiv.org/pdf/2408.13095.

96. Kajale, S. N., Nguyen, T., Hung, N. T., Li, M. & Sarkar, D. Field-free deterministic switching of all–van der Waals spin-orbit torque system above room temperature. *Sci. Adv.* **10**, eadk8669 (2024).

97. Abdukayumov, K. et al. Atomic-layer controlled transition from inverse Rashba-Edelstein effect to inverse Spin Hall effect in 2D $PtSe_2$ probed by THz spintronic emission. *Adv. Mater.* **36**, e2304243 (2024).

98. Xu, H. et al. High spin hall conductivity in large-area type-II dirac semimetal $PtTe_2$. *Adv. Mater.* **32**, e2000513 (2020).

99. Wang, F. et al. Field-free switching of perpendicular magnetization by two-dimensional $PtTe_2$/WTe_2 van der Waals heterostructures with high spin Hall conductivity. *Nat. Mater.* **23**, 768–774 (2024).

100. MacNeill, D. et al. Thickness dependence of spin-orbit torques generated by WTe_2. *Phys. Rev. B* **96**, 054450 (2017).

101. Yang, Q. et al. Field-free spin-orbit torque switching in ferromagnetic trilayers at sub-ns timescales. *Nat. Commun.* **15**, 1814 (2024).

102. Wu, H. et al. Room-temperature spin-orbit torque from topological surface states. *Phys. Rev. Lett.* **123**, 207205 (2019).

103. Mak, K. F. & Shan, J. Semiconductor moire materials. *Nat. Nanotechnol.* **17**, 686–695 (2022).

104. Andrei, E. Y. et al. The marvels of moiré materials. *Nat. Rev. Mater.* **6**, 201–206 (2021).
105. Zhang, Y., Yuan, N. F. Q. & Fu, L. Moiré quantum chemistry: charge transfer in transition metal dichalcogenide superlattices. *Phys. Rev. B* **102**, 201115(R) (2020).
106. Arora, H. S. et al. Superconductivity in metallic twisted bilayer graphene stabilized by WSe_2. *Nature* **583**, 379–384 (2020).
107. Kang, K. et al. Evidence of the fractional quantum spin Hall effect in moire $MoTe_2$. *Nature* **628**, 522–526 (2024).
108. Xiao, D., Yao, W. & Niu, Q. Valley-contrasting physics in graphene: magnetic moment and topological transport. *Phys. Rev. Lett.* **99**, 236809 (2007).
109. Tao, Z. et al. Giant spin Hall effect in AB-stacked $MoTe_2$/WSe_2 bilayers. *Nat. Nanotechnol.* **19**, 28–33 (2024).
110. Adak, P. C., Sinha, S., Agarwal, A. & Deshmukh, M. M. Tunable moiré materials for probing Berry physics and topology. *Nat. Rev. Mater.* **9**, 481–498 (2024).
111. Li, T. et al. Quantum anomalous Hall effect from intertwined moire bands. *Nature* **600**, 641–646 (2021).
112. Wu, F., Lovorn, T., Tutuc, E., Martin, I. & MacDonald, A. H. Topological insulators in twisted transition metal dichalcogenide homobilayers. *Phys. Rev. Lett.* **122**, 086402 (2019).
113. Deng, Y. et al. Quantum anomalous Hall effect in intrinsic magnetictopological insulator $MnBi_2Te_4$. *Science* **367**, 895–900 (2020).
114. Tschirhart, C. L. et al. Intrinsic spin Hall torque in a moiré Chern magnet. *Nat. Phys.* **19**, 807–813 (2023).
115. Han, T. et al. Large quantum anomalous Hall effect in spin-orbit proximitized rhombohedral graphene. *Science* **384**, 647 (2024).
116. Huang, B. C. et al. Layer-dependent ferromagnetism in a van der Waals crystal down to the monolayer limit. *Nature* **546**, 270–273 (2017).
117. Gong, C. et al. Discovery of intrinsic ferromagnetism in two-dimensional van der Waals crystals. *Nature* **546**, 265–269 (2017).
118. Safeer, C. K. et al. Room-temperature spin Hall effect in graphene/MoS_2 van der Waals heterostructures. *Nano Lett.* **19**, 1074–1082 (2019).

Author contributions
A.A. conceived the review's outline and structured the paper. Z.Z. and Y.L. drafted the initial manuscript, which A.A. subsequently polished and proofread. All authors have reviewed and approved the final content.

Competing interests
The authors declare no competing interests.

Additional information
Correspondence and requests for materials should be addressed to Ahmet Avsar.

Reprints and permissions information is available at http://www.nature.com/reprints

Publisher's note Springer Nature remains neutral with regard to jurisdictional claims in published maps and institutional affiliations.